

Bubble capture by a propeller

By FRANÇOIS CAILLÉ¹, CHRISTOPHE CLANET¹
AND JACQUES MAGNAUDET²

¹IRPHE, UMR 6594, 49 rue F. Joliot-Curie, BP 146, 13384 Marseille, France

²IMFT, Allée du Professeur Camille Soula, 31400, Toulouse, France

(Received 15 February 2006 and in revised form 20 April 2006)

A small air bubble (radius a) is injected in water (kinematic viscosity ν) in the vicinity (distance r_0) of a propeller (radius r_p , angular frequency ω). We study experimentally and theoretically the conditions under which the bubble can be ‘captured’, i.e. deviated from its vertical trajectory (imposed by gravity g) and moved toward the centre of the propeller ($r = 0$). We show that the capture frequency ω_{capt} follows the relationship

$$\omega_{capt} = \left(\frac{2ga^2}{9\beta\nu r_p f(Re_b)} \right) \left(\frac{r_0}{r_p} \right)^2 (1 + \cos \varphi_0),$$

where β is a dimensionless parameter characterizing the propeller, $f(Re_b)$ is an empirical correction to Stokes’ drag law which accounts for finite-Reynolds-number effects and $\pi/2 - \varphi_0$ is the angle between the axis of the propeller and the line between the centre of the propeller and the point where the bubble is injected. This law is found to be valid as long as the distance d between the propeller and the water surface is larger than $3r_0$. For smaller distances, the capture frequency increases; using an image technique, we show how the above expression is modified by the presence of the surface.

1. Introduction

Ship wake usually refers to the classical Kelvin wave system observed behind surface vessels and characterised by a well-known constant angle of 39° (Kelvin 1887; Lighthill 1978). As they cruise, surface vessels also entrain air and produce a bubbly wake, illustrated in figure 1. The width of this wake typically scales with the width of the vessel, whereas its length may extend up to one hundred ship lengths. The presence of bubbles behind the ship changes the speed of sound in the water (Batchelor 1967; Landau & Lifshitz 1959) and associates a strong acoustic signature to the motion of the ship (NDRC 1946; Crighton & Ffowcs Williams 1969; Marmorino & Trump 1996). Many studies have been dedicated to the acoustical properties of bubbly wakes (Trevorrow, Vagle & Farmer 1994) as well as to the origin of the bubbles: cavitation (Weitendorf 2001), bow wave (Waniewski, Brennen & Raichlen 2002; Zhu, Oguz & Prosperetti 2000), etc.

While the role of the propeller has long been recognized in the generation of cavitation bubbles, its importance with respect to the bubbly far wake (several vessel lengths downstream) does not seem to have been reported. Its effect is illustrated in figure 1 where a two-propeller vessel produces a bubbly far wake composed of two ‘white lines’ (figure 1a) whereas a vessel using a single propeller produces only one

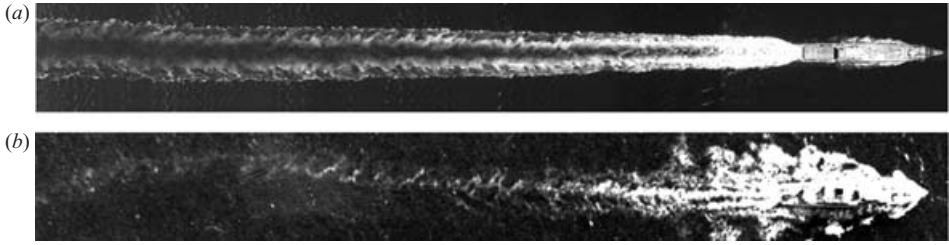


FIGURE 1. Airplane visualization of bubble wakes: (a) TCD Foudre (<http://www.netmarine.net/bat/tcd/foudre/caracter.htm>) with two propellers, (b) CMT Lyre (<http://www.netmarine.net/bat/cm/lyre/caracter.htm>) with one propeller.

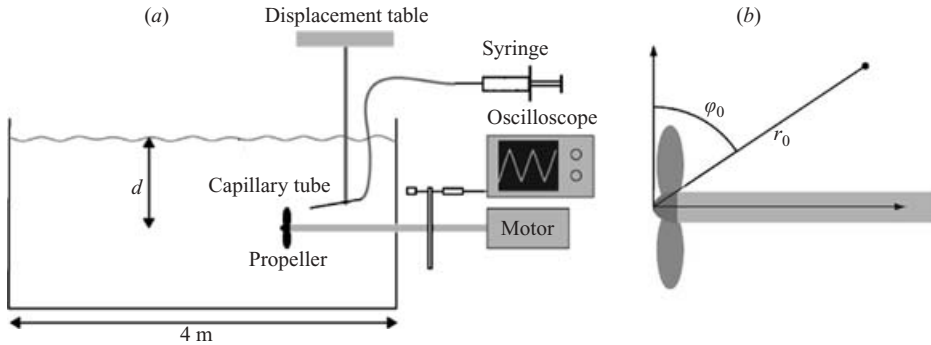


FIGURE 2. Experimental set-up: (a) sketch of the experiment, (b) definition of the injection location.

white line (figure 1*b*). This observation shows that the propeller catches the bubbles around it and plays a major role in the structure of the bubbly far wake. This mechanism predominates in the formation of bubbly far wakes in water with a low concentration of dissolved gas, where cavitation does not occur. The present study considers the role of the propeller in this capture process. In order to elucidate the physical laws governing the capture, we drastically simplify the problem and reduce it to a laboratory experiment in which we examine the capture of a bubble by a propeller (radius r_p , angular frequency ω), rotating in a tank where the fluid is at rest. The study is conducted in water (kinematic viscosity ν), in the high-Reynolds-number regime ($Re \equiv r_p^2 \omega / \nu \gg 1$) and with air bubbles (radius a) corresponding to a low Galilé number ($Ga \equiv ga^3 / \nu^2 < 1$).

2. Experimental set-up and protocol

The experimental set-up is sketched in figure 2(*a*): the propeller is immersed at a depth d below the free surface in a 4 m long tank with a 1 m^2 cross-section filled with tap water. A typical experiment first consists of injecting air bubbles in water at rest (propeller at rest) at a controlled location (r_0, φ_0) defined in figure 2(*b*). Once a constant bubbly regime is achieved (figure 3*a*), the rotation speed of the propeller is increased (figure 3*b*) until the capture (figure 3*c, d*). The capture frequency ω_{capt} is stored and the experiment is repeated with a different bubble size a , injection location (r_0, φ_0) and propeller position d .

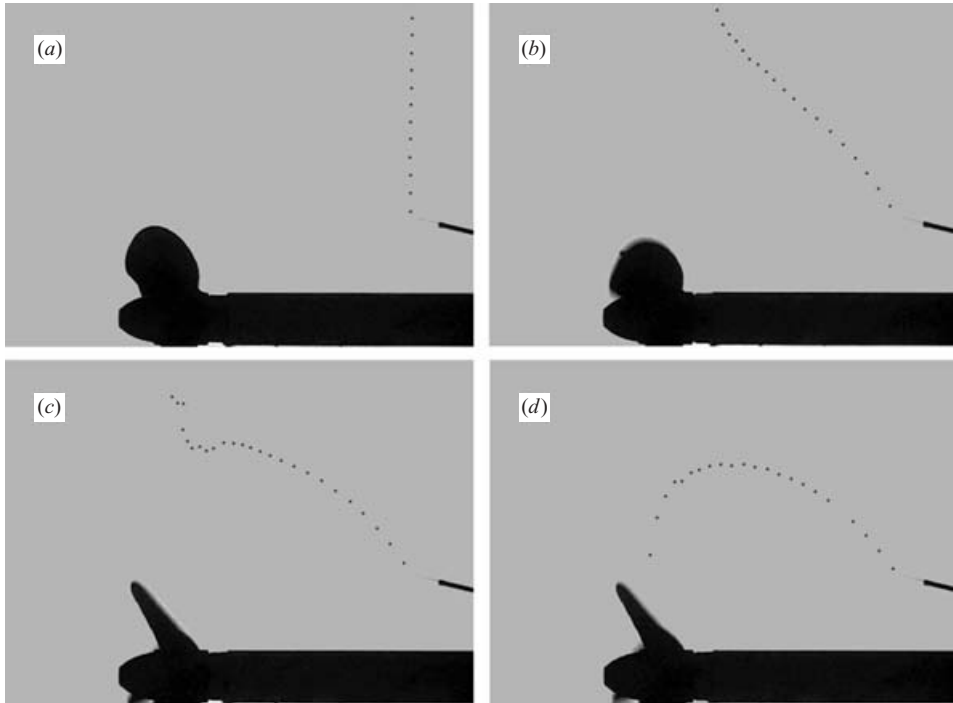


FIGURE 3. Example of a typical experiment: (a) constant bubbling regime without propeller rotation $\omega=0$, (b) deviation of the vertical bubble trajectory for ‘moderate’ rotation $\omega < \omega_{capt}$, (c) deflection of the vertical motion near the transition to the capture $\omega \sim \omega_{capt}$, (d) capture of the bubbles in the ‘high’ rotation regime $\omega > \omega_{capt}$.

We use a three-blade brace propeller ($r_p = 20$ mm) designed for model boats and commercialized by RIVABO, driven by a 12 V GRAUPNER electric motor powered by a DC power supply allowing a maximum rotation speed of approximately 600 rad s^{-1} (~ 6000 RPM). The rotation speed is measured using an optical coder made of a laser impinging on a photodiode. The laser beam is interrupted once per revolution resulting in a periodic output signal from the photodiode whose frequency is then directly obtained using a digital oscilloscope.

In order to study the influence of the bubble size on the capture angular speed, glass capillary tubes of various diameters are used to create air bubbles with radii ranging from 100 to 250 μm . The air flux is regulated with a KS200 syringe-pump. The size of the bubbles is known to be influenced by the flow created by the propeller (Kulkarni & Joshi 2005). For this reason, when the rotation speed is varied, the size of the bubbles is systematically measured at the exit of the capillary tube by an optical system composed of a LEICA MZ16 binocular coupled with a KODAK high-speed video camera running at 4500 frames per second. The resolution of the ensemble is 300 pixels per mm at a working distance of 35 cm.

The bubble spacing is chosen large enough to avoid interaction between successive bubbles (Katz & Meneveau 1996) and the bubble trajectory ($r(t), \varphi(t)$) is always observed to remain in a vertical plane.

To characterize the dependence of the capture frequency on the injection location, the capillary tubes are mounted on a 3-axis displacement table.

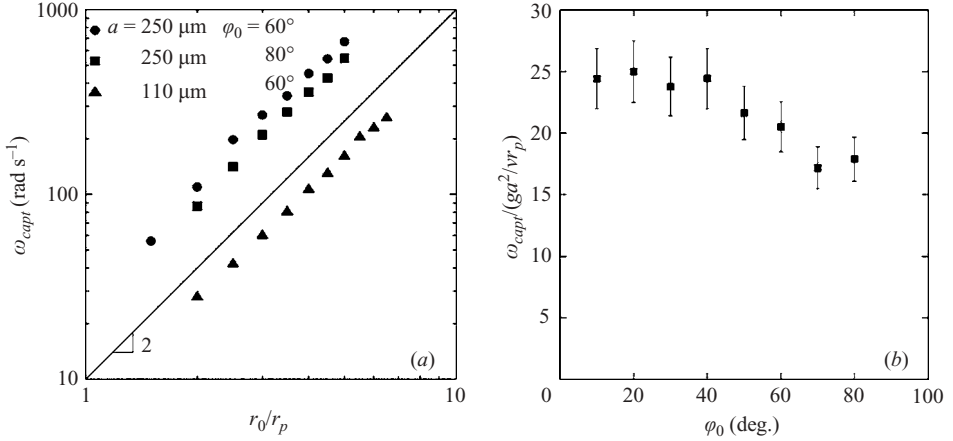


FIGURE 4. (a) Evolution of the capture frequency ω_{capt} with the reduced distance from injection r_0/r_p , for various bubble radii a and injection angles φ_0 . (b) Evolution of the reduced capture frequency $\omega_{capt}/(ga^2/(\nu r_p))$ with the injection angle φ_0 for a constant reduced distance $r_0/r_p = 4$.

3. Experimental results

The evolution of the capture frequency ω_{capt} with the reduced injection distance r_0/r_p is displayed in figure 4(a) for different polar angles φ_0 and bubble radii a . For a given bubble size a and injection angle φ_0 , the capture frequency increases as the square of the distance. Note also that ω_{capt} is highly sensitive to the bubble size: for the same injection position, figure 4(a) shows that the capture frequency is multiplied by a factor of five when the bubble size is multiplied by 2.15. Finally, figure 4(b) also reveals that the capture frequency ω_{capt} slowly changes with the injection angle φ_0 .

4. Model

4.1. Scaling arguments

Scaling arguments can partly explain the experimental trends revealed by figure 4(a). As a first approximation, let us assume that the motion of a bubble is mainly governed by the buoyancy force B and the drag force D . In contrast to the case of a bubble rising in a liquid at rest, where the drag force is purely vertical, the propeller inflow induces a horizontal component in this force. We guess that a bubble is captured if this horizontal component, evaluated at the injection point, has the same order of magnitude as the buoyancy force. For small bubbles of radius a in the Stokes regime, the drag force is $D \sim \mu U a$ where μ is the dynamic viscosity of water and U is the slip velocity between the bubble and the flow induced by the propeller at the bubble location. The buoyancy force is $B \sim \rho g a^3$ where ρ is the water density and g denotes acceleration due to gravity. At the injection point we can then write $\mu U_0 a \sim \rho g a^3$. If we assume that the flow created by the propeller can be modelled by a sink of strength $Q \sim r_p^3 \omega_{capt}$ we can recast the above drag force in the form $\mu a Q / r_0^2$, which yields

$$\omega_{capt} \sim \left(\frac{ga^2}{\nu r_p} \right) \left(\frac{r_0}{r_p} \right)^2. \quad (4.1)$$

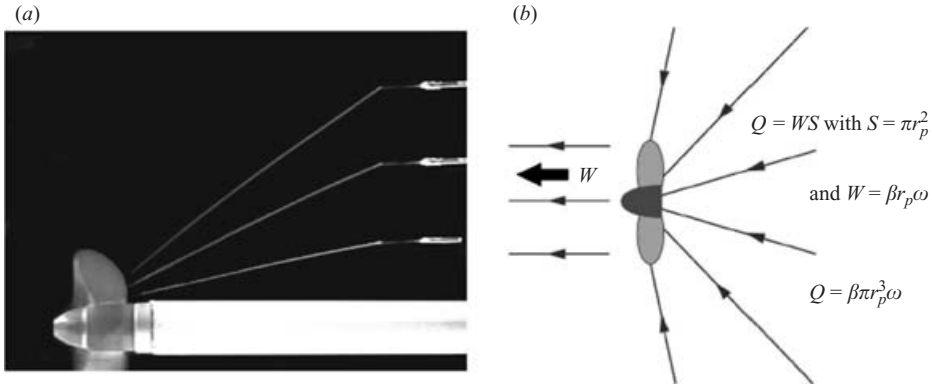


FIGURE 5. (a) Visualizations of the streaklines using fluorescein. (b) Notation for the inflow model.

According to the experimental results in figure 4(a), this scaling argument provides the correct evolution of ω_{capt} with the injection distance as well as a realistic dependence on the bubble size. But this simple model does not account for the dependence on the polar angle of injection revealed by figure 4(b), which shows that the reduced capture frequency decreases when the injection angle increases and is lowered by a factor of 1.6 when φ_0 increases from 10° to 80° .

A more refined model is thus required to fully predict the dependence of the angular capture speed on the various parameters of the problem.

4.2. Propeller inflow

Figure 5(a) shows some fluorescein visualizations of the inflow created by the propeller. This technique reveals that the streaklines are purely radial. Moreover, since the flow is steady, the streaklines are also streamlines and the flow can thus be written in the form $\mathbf{U} = U(r)\mathbf{e}_r$. These visualizations and all the measurements reported in this paper were performed over a time smaller than the characteristic diffusion time ($r_0^2/\nu \approx 20$ min). By Kelvin's theorem, the inflow region may thus be considered as irrotational at all times relevant in the experiments. Therefore we are in position to use an irrotational approximation to express $U(r)$.

Moreover, for injection distances much larger than the propeller radius r_p , it is reasonable to approximate the propeller inflow as a point-sink flow:

$$U(r) = -\frac{Q}{2\pi r^2}, \quad (4.2)$$

where Q is the sink strength. Dimensional considerations imply $Q \sim r_p^3 \omega$ where ω is the propeller angular speed. Therefore we model the propeller inflow by a point-sink flow of strength $Q = \beta \pi r_p^3 \omega$, where β is a coefficient depending on the propeller characteristics (see figure 5b for details).

Let us remark on the modelling of the flow created by the propeller. Owing to mass conservation, a 'natural' model could have been a dipole. This is the case at low Reynolds number. However, at high Reynolds number the propeller produces a thrust, which is not compatible with a dipole. In this regime, the sink/source symmetry is broken and the propeller behaves as a laminar sink for a large part of its surroundings and as a turbulent jet for the remaining part. Since we are only concerned with the upstream region of the propeller, we only discuss here the laminar

sink domain and verify experimentally that the streamlines (figure 5a) are straight rays (which would not have been the case with a dipole).

4.3. Bubble trajectory

Neglecting the bubble density with respect to the water density ρ , the equation of motion of a bubble of radius a and volume \mathcal{V} moving at velocity \mathbf{V} in an irrotational flow of velocity \mathbf{U} is (Magnaudet & Eames 2000)

$$\rho\mathcal{V}C_M\frac{d\mathbf{V}}{dt} = \rho C_D\frac{\pi a^2}{2}\|\mathbf{U} - \mathbf{V}\|(\mathbf{U} - \mathbf{V}) + \rho\mathcal{V}(1 + C_M)\frac{D\mathbf{U}}{Dt} - \rho\mathcal{V}\mathbf{g}, \quad (4.3)$$

where C_D and C_M stand for the drag and added-mass coefficients, respectively, and D/Dt denotes the material derivative.

For a spherical particle C_M is known to be $1/2$ and (4.3) may be rewritten in the form

$$\frac{d\mathbf{V}}{dt} = \frac{9\nu}{a^2}f(Re)(\mathbf{U} - \mathbf{V}) + 3\frac{D\mathbf{U}}{Dt} - 2\mathbf{g}, \quad (4.4)$$

where $Re = 2a\|\mathbf{U} - \mathbf{V}\|/\nu$ and $f(Re)$ is an empirical correction to Stokes' drag law which accounts for finite-Reynolds-number effects (in what follows we use the standard Schiller–Neumann correction $f(Re) = 1 + 0.15Re^{0.687}$ (Clift, Grace & Weber 1978)). We select an expression for C_D appropriate to rigid spheres rather than to clean bubbles because our experiments are carried out in tap water which is known to contain impurities. Therefore, small bubbles may reasonably be approximated by rigid spheres (Magnaudet & Eames 2000).

In a quiescent fluid, the bubble would rise with a speed $\mathbf{V}_b \equiv -2ga^2f^{-1}(Re_b)/9\nu$, with $Re_b = 2a\|\mathbf{V}_b\|/\nu$. In other words the terminal Reynolds number Re_b is such that $Re_b f(Re_b) = 4ga^3/9\nu^2$. Introducing the rising speed \mathbf{V}_b , (4.4) simplifies to

$$\frac{d\mathbf{V}}{dt} = \frac{\mathbf{V}_b}{\tau} + \frac{\mathbf{U} - \mathbf{V}}{\tau'} + 3\frac{D\mathbf{U}}{Dt}, \quad (4.5)$$

where $\tau' = a^2f^{-1}(Re)/9\nu$ and $\tau \equiv a^2f^{-1}(Re_b)/9\nu$. Due to the weak sensitivity of τ' to the Reynolds number, we assume in the following $\tau' \simeq \tau$. In a steady uniform flow \mathbf{U} , this means that the bubble velocity \mathbf{V} tends towards the constant velocity $\mathbf{V}_b + \mathbf{U}$ with a characteristic time τ .

For the sink flow $\mathbf{U} = U(r)\mathbf{e}_r$, this equation takes the form

$$\frac{d\mathbf{V}}{dt} = \frac{\mathbf{V}_b + (1 + \tau/\tau_e)\mathbf{U} - \mathbf{V}}{\tau}, \quad (4.6)$$

where $1/\tau_e \equiv 3dU/dr$, τ_e being the local characteristic variation time of the inflow velocity.

The ratio τ/τ_e in (4.6) measures the ability of the bubble to adapt to the flow variations: if $\tau/\tau_e \ll 1$, the bubble adapts its speed almost instantaneously to the external conditions, since during its reaction time τ the flow remains almost uniform. In the other limit, $\tau/\tau_e \gg 1$, the flow varies well before the bubble adapts its speed and the bubble never reaches an equilibrium state.

In our case, using expression (4.2) for the propeller inflow \mathbf{U} , the ratio τ/τ_e is

$$\frac{\tau}{\tau_e} \approx \frac{\beta r_p^3 \omega a^2 f^{-1}(Re_b)}{3\nu r^3}. \quad (4.7)$$

In the propeller region ($r \approx r_p$), equation (4.7) becomes $\tau/\tau_e \approx \beta \omega a^2 f^{-1}(Re_b)/3\nu \approx 0.09$ for a bubble of 100 μm radius and a rotation speed of 100 rad s^{-1} , and using the

measured value $\beta \approx 0.2$. However this time ratio decreases as r^{-3} . Therefore in the above example it is reduced to 1.1×10^{-2} for $r/r_p = 2$. Thus, under the conditions of the present experiments, we may consider that the adaptation time of the bubble is small compared to the characteristic time of the flow variation, except in the immediate vicinity of the propeller. Therefore, (4.6) may be simplified to

$$\frac{d\mathbf{V}}{dt} = \frac{\mathbf{V}_b + \mathbf{U} - \mathbf{V}}{\tau}. \quad (4.8)$$

Hence, the bubble velocity \mathbf{V} reaches the local velocity $\mathbf{V}_b + \mathbf{U}$ after a time of the order of τ . As $\tau/\tau_e \ll 1$, the transient stage of the motion may be neglected and we can write the bubble velocity as a function of position only in the form

$$\mathbf{V} \simeq \mathbf{V}_b + \mathbf{U}. \quad (4.9)$$

The bubble velocity is the sum of two velocities that can both be derived from elementary solutions of Laplace's equation. Noting that the problem is symmetric about the vertical (z) axis, we can introduce the so-called Stokes streamfunction Ψ suitable for axisymmetric problems solved in spherical coordinates and split it into the form

$$\Psi = \Psi_b + \Psi_p$$

where

$$\Psi_b = \frac{1}{2} V_b r^2 \sin^2 \varphi, \quad \Psi_p = \frac{Q}{2\pi} \cos \varphi.$$

Bubble trajectories are given by iso- Ψ curves. Therefore the coordinates (r, φ) of a bubble initially released at (r_0, φ_0) must satisfy the condition $\Psi(r, \varphi) = \Psi(r_0, \varphi_0)$. The problem is now similar to a Rankine solid body problem (Lamb 1932).

The corresponding trajectories are presented in figure 6(a). For a given sink strength and bubble size we can define a capture zone (dark region in figure 6a) enclosing the injection points for which bubbles are captured. The equation of the envelope \mathcal{E} is given by $r = \sqrt{Q(1 - \cos \varphi)/(\pi V_b \sin^2 \varphi)}$.

The capture frequency ω_{capt} is the value of ω for which the envelope passes through the injection point with coordinates (r_0, φ_0) . Replacing Q and V_b by their expressions above we obtain

$$\omega_{capt} \sim \omega_0 f^{-1}(Re_b) \left(\frac{r_0}{r_p} \right)^2 (1 + \cos \varphi_0) \quad (4.10)$$

with $\omega_0 = ga^2/vr_p$.

4.4. Comparison with experiments

The evolution with $f^{-1}(Re_b)(r_0/r_p)^2(1 + \cos \varphi_0)$ of the reduced capture frequency ω_{capt}/ω_0 is shown in figure 6(b). The different experimental sets collapse onto a single curve and the linearity predicted by equation (4.10) is achieved for all experimental conditions. The prefactor $2/(9\beta)$ is found to be of order unity (1.3).

5. Influence of the free surface

All the results reported so far have been obtained in the 'deep' limit where the distance r_0 between the bubble and the propeller is small compared to the distance d between the propeller and the free surface (figure 7a). The corresponding capture frequency, described by (4.10) is now referred to as $\omega_{capt-\infty}$ and we study what happens when the ratio r_0/d decreases.

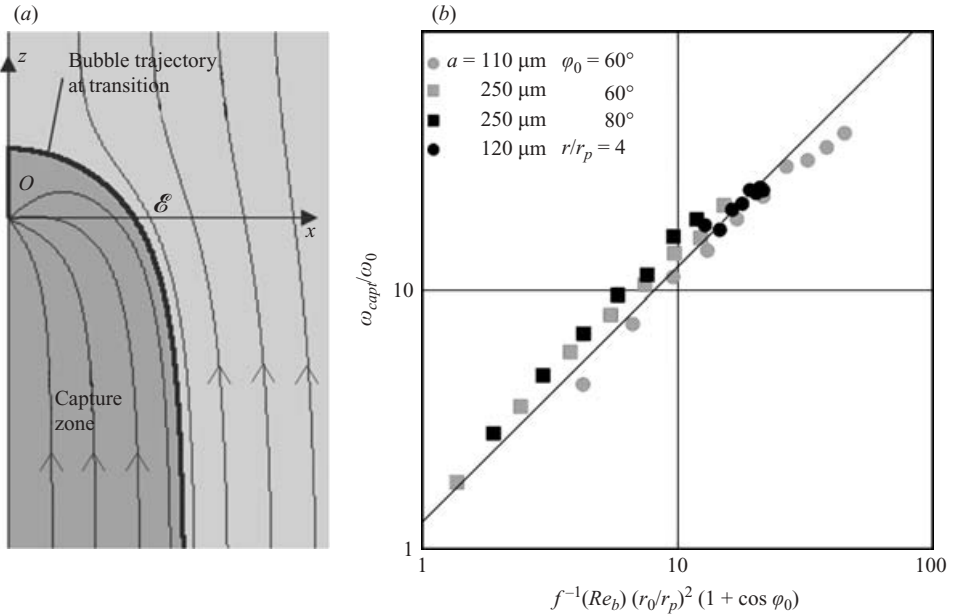


FIGURE 6. (a) Theoretical trajectories of the bubbles and envelope \mathcal{E} described in §4.3. (b) Comparison between the reduced capture frequency obtained theoretically (4.10) and the experimental measurements.

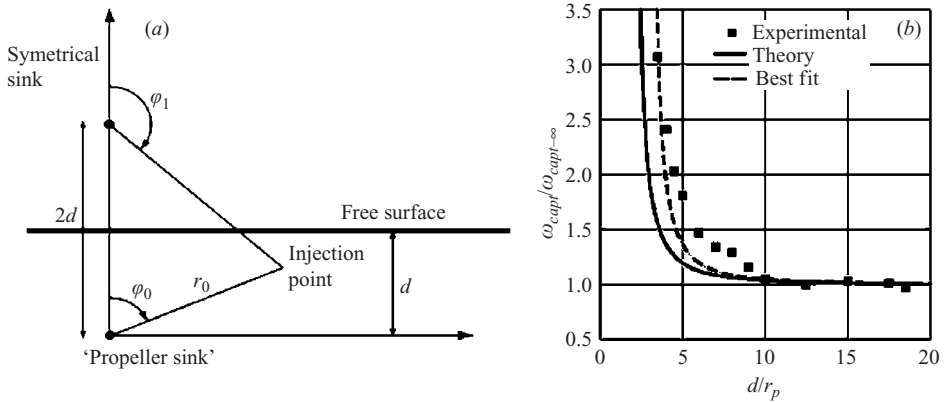


FIGURE 7. (a) Model for the free-surface effect. (b) Evolution of the reduced capture frequency $\omega_{capt}/\omega_{capt-\infty}$ as a function of d/r_p . The location of the injection point is fixed ($r_0/r_p = 4$, $\phi_0 = 60^\circ$).

5.1. Experimental evidence

Figure 7(b) presents the evolution of the reduced capture frequency $\omega_{capt}/\omega_{capt-\infty}$ with the reduced distance d/r_p between the free surface and the propeller, where the injection point is maintained at a fixed position: $r_0/r_p = 4$ and $\phi_0 = 60^\circ$. This figure reveals that the capture frequency increases when the distance between the free-surface and the propeller decreases. In this example, the ‘deep’ limit, $\omega_{capt}/\omega_{capt-\infty} \approx 1$ is reached for $d > 10r_p$.

5.2. Modification of the model

To introduce the effect of the free surface into our irrotational model we add an ‘image’ propeller to the actual one (figure 7a). Mathematically, this is achieved by adding an image streamfunction Ψ_i to the initial model. Thus we now have

$$\Psi = \Psi_b + \Psi_p + \Psi_i$$

where

$$\Psi_b = \frac{1}{2} V_b r^2 \sin^2 \varphi, \quad \Psi_p = \frac{Q}{2\pi} \cos \varphi, \quad \Psi_i = \frac{Q}{2\pi} \frac{r \cos \varphi - 2d}{\sqrt{r^2 + 4d^2 - 4rd \cos \varphi}}.$$

Duplicating the previous approach, we obtain the capture frequency of a bubble of radius a injected at the location (r_0, φ_0) in the form

$$\frac{\omega_{capt}}{\omega_{capt-\infty}} = \frac{1 - \cos \varphi_0}{-\cos \varphi_1 - \cos \varphi_0}. \quad (5.1)$$

In the ‘deep’ limit, $\varphi_1 \rightarrow \pi$ and (5.1) tends toward 1. For a bubble on the surface, $\varphi_1 = \pi - \varphi_0$ and the capture frequency goes to infinity: bubbles located on the surface cannot be captured since they are equally attracted by the propeller and its image. The result corresponding to (5.1) is displayed with a solid line in figure 7(b). While the model and the experimental data follow the same qualitative trend, the experimental values of ω_{capt} diverge for distances to the surface larger than those predicted theoretically. We attribute this difference to a finite-size effect: the actual position of the theoretical point sink which models the propeller is experimentally defined up to an error of the order of r_p since the distance between the free surface and the propeller cannot be smaller than r_p . To take this effect into account, we introduce an effective distance between the surface and the propeller $d' = d - \lambda r_p$ depending on a parameter λ . The best fit between the theoretical curve and the experimental data is obtained for $\lambda = 1$ (dashed line in figure 7b).

The above model holds provided the deformation h of the surface remains small compared to the distance d . If U is the characteristic velocity at the surface, we evaluate $h \approx U^2/g$, and $h/d \approx U^2/gd$. In our case, $U \approx \beta r_p^3 \omega/d^2$ and we deduce $h/d \approx r_p^6 \beta^2 \omega^2/(gd^5)$. The model thus applies in the limit $d/r_p \gg (r_p \beta^2 \omega^2/g)^{1/5}$, a criterion satisfied for the data presented in figure 7(b).

6. Conclusion

We have carried out an experimental and theoretical investigation of the capture of ‘small’ air bubbles by a propeller embedded in water at rest. In the ‘deep’ limit ($d/r_p \geq 10$) we find that the capture frequency is given by equation (4.10) and thus changes with the size of the bubble a , injection distance from the propeller r_0 and also, in a more subtle way, with the angular injection location φ_0 . We have first quantified these three dependences experimentally and then derived them theoretically using a potential flow approach. The main theoretical idea is that for ‘small’ bubbles, the bubble velocity V is merely the sum of the velocity imposed by the propeller U and the rise velocity in a liquid at rest ($V_b \equiv -2ga^2 f^{-1}(Re_b)/9\nu$). This velocity representation allowed us to superimpose the corresponding streamfunctions and to determine bubble trajectories as well as the envelope of the capture zone.

In the ‘shallow’ situation ($d/r_p < 10$), we found that the capture is made less likely by the presence of the free-surface. We used an image approach to account for the

free-surface effect and showed that the modified capture frequency is in fairly good agreement with the experimental measurements.

This approach can be adapted to more complicated configurations, by replacing the sink flow induced by the propeller by the actual flow in the region surrounding the propeller area. Situations involving more than one propeller may also be analysed in the same way. However the symmetry with respect to the vertical direction will then be lost, and the streamfunction approach will have to be replaced by a direct computation of the three-dimensional bubble trajectories.

We thank Xavier Lenhardt who impuled this study, J.P. Moretto for providing real data and J.-M. Quenez and O. Perelman for improving our understanding of naval construction constraints.

REFERENCES

- BATCHELOR, G. K. 1967 Compression waves in a suspension of gas bubbles in a liquid. *Proc. 8th Symposium on Advanced Problems and Methods in Fluid Mechanics, Tarda, Poland*.
- CLIFT, R., GRACE, J. R. & WEBER, M. E. 1978 *Bubbles, Drops and Particles*. Academic.
- CRIGHTON, D. G. & FFWCS WILLIAMS, J. E. 1969 Sound generation by turbulent two-phase flow. *J. Fluid Mech.* **36**, 585–603.
- KATZ, J. & MENEVEAU, C. 1996 Wake-induced relative motion of bubbles rising in line. *Intl J. Multiphase Flow* **22**, 239–258.
- KELVIN, LORD 1887 On ship waves. *Proc. Inst. Mech. Engrs* 409–433.
- KULKARNI, A. A. & JOSHI, J. B. 2005 Bubble formation and bubble rise velocity in gas-liquid systems: a review. *Ind. Engng Chem. Res.* **44**, 5873–5931.
- LAMB, H. 1932 *Hydrodynamics*. Cambridge University Press.
- LANDAU, L. & LIFSHITZ, E. M. 1959 *Fluid Mechanics*. Pergamon Press.
- LIGHTHILL, J. 1978 *Waves in Fluids*. Cambridge University Press.
- MAGNAUDET, J. & EAMES, I. 2000 The motion of high-Reynolds-number bubbles in inhomogeneous flows. *Annu. Rev. Fluid Mech.* **32**, 659–708.
- MARMORINO, G. O. & TRUMP, C. L. 1996 Preliminary side-scan ADCP measurements across a ship's wake. *J. Atmosp. Ocean Tech.* **13**, 507–513.
- NDRC 1946 Physics of sound in the sea. *National Defense Research Committee Division 6, Summary Tech. Rep.* Vol. 8, reprinted 1969 as *NAVMAT Rep.* P-9675.
- TREVORROW, M. V., VAGLE, S. & FARMER, D. M. 1994 Acoustical measurements of microbubbles within ship wakes. *J. Acoust. Soc. Am.* **95**, 1922–1930.
- WANIEWSKI, T. A., BRENNEN, C. E. & RAICHLIN, F. 2002 Bow wave dynamics. *J. Ship Res.* **46**, 1–15.
- WEITENDORF, E. A. 2001 On the history of propeller cavitation and cavitation tunnels. *CAV 2001: Fourth Intl Symposium on Cavitation, June 20–23*.
- ZHU, Y., OGUZ, H. N. & PROSPERETTI, A. 2000 On the mechanism of air entrainment by liquid jets at a free surface. *J. Fluid Mech.* **404**, 151–177.